Temperature-dependent cross sections of O_2–O_2 collision-induced absorption resonances at 477 and 577 nm

Maarten Sneep[1], Dmitry Ityaksov, Ilse Aben[2], Harold Linnartz[3], Wim Ubachs*

Laser Centre, Vrije Universiteit, De Boelelaan 1081–1083, 1081 HV, Amsterdam, The Netherlands

Abstract

Two collision-induced absorption features of oxygen have been investigated by means of the laser-based cavity ring-down technique at pressures between 0 and 1000 hPa and at temperatures in the range 184–294 K. Peak cross sections, resonance widths and integrated cross sections, as well as spectral profiles, have been determined for the broad O_2–O_2 resonances centered at 477 and 577 nm. Results are compared with previous measurements to establish an updated temperature dependence for the cross sections of both resonances, yielding integrated cross sections, that exhibit a minimum near 200 K and that increase in a near-linear fashion in the atmospherically relevant range of 200–300 K. A significant increase in the widths of the resonance profiles upon temperature increase is firmly established. Parameters and temperature-dependent trends for the shape and strengths of the resonances are produced, that can be implemented in cloud retrieval in atmospheric Earth observation.
© 2005 Elsevier Ltd. All rights reserved.

*Corresponding author. Tel.: + 31 20 5987948; fax: + 31 20 5987999.
  E-mail addresses: sneep@nat.vu.nl (M. Sneep), ityaksov@nat.vu.nl (D. Ityaksov), i.aben@sron.nl (I. Aben), linnartz@few.vu.nl (H. Linnartz), wimu@nat.vu.nl (W. Ubachs).
  [1]Present address: Climate Research and Seismology Department, Royal Netherlands Meteorological Institute (KNMI), De Bilt, The Netherlands.
  [2]Also at: Netherlands Institute for Space Research, Utrecht, The Netherlands.
  [3]Also at: Sackler Laboratory for Astrophysics, Leiden Observatory, Leiden, The Netherlands.

1. Introduction

The oxygen molecule has a series of collision-induced absorption (CIA) resonances, involving molecular pairs that jointly absorb a single photon, whereby *both* molecules undergo a transition to an electronically excited state. These resonances were discovered in the study of liquid oxygen in 1933 by Ellis and Kneser [1], and even that early—just a few years after the advent of molecular quantum mechanics—were understood as bi-molecular absorptions and could correctly be assigned in terms of quantum numbers. The resonance at 477 nm is assigned as an excitation of two oxygen ground-state molecules, one into the $a\,^1\Delta_g(v=0)$ state and one into the $b\,^1\Sigma_g^+(v=0)$ state. The resonance near 577 nm can be assigned to the transition $a\,^1\Delta_g(v=0) + a\,^1\Delta_g(v=1) \leftarrow X\,^3\Sigma_g^-(v=0) + X\,^3\Sigma_g^-(v=0)$. The absorption strength of the collision-induced features is rather high, when compared to monomer absorption, because these phenomena are associated with symmetry breaking. Whereas, the O_2 molecule is homonuclear and exhibits no dipole moment, all three lowest electronic states connected in the visible spectrum of oxygen have *gerade* symmetry, and hence transitions between these states are highly forbidden. Binary collisions give rise to distortions of the electronic wave functions and to a breaking of the inversion symmetry, which then permits optical transitions. It is noted further that the two collision-induced features at 477 and 577 nm are not associated with a monomer absorption at the same wavelengths; that would contradict the distribution of excitation energy over the two collision partners. The fact that the 577 nm resonance overlaps the $b\,^1\Sigma_g^+ - X\,^3\Sigma_g^-(3,0)$ monomer band is a happenstance coincidence. As was discussed by Naus and Ubachs [2], the interference of both phenomena can be avoided experimentally.

Atmospheric observations of the features related to O_2-CIA date back to the 19th century [3]. Since then a large number of laboratory investigations have been pursued to quantitatively assess the cross sections related to the collisional absorption features. Accurate results in the high-pressure regime were obtained by Dianov–Klokov [4] and Greenblatt et al. [5], while focus on low-temperature effects prevailed in the studies by Ewing and coworkers [6,7]. Perner and Platt [8] performed measurements on atmospheric absorptions at long path length, Pfeilsticker et al. [9] determined altitude profile spectral features of $(O_2)_2$ absorption bands from balloon observations, and Wagner et al. [10] detected the oxygen collisional features in the Earth's atmosphere against the moonlight. In Ref. [9] a value for the enthalpy of formation of the O_4 complex was derived, in good agreement with findings from molecular scattering experiments [11,12].

Besides these investigations on the *electronic* CIA features observable in the visible wavelength range, oxygen collisional features were also studied at longer wavelengths, and there exists an extensive literature on this subject. For the 6 μm vibrational excitation we cite the laboratory investigations by Orlando et al. [13] and Baranov et al. [14]. The same vibrational CIA band was investigated under stratospheric conditions with use of a balloon-borne FT-interferometer by Rinsland et al. [15]. In the far-infrared domain oxygen exhibits a translation–rotation spectrum with collisional features, which was investigated experimentally by Bosomworth and Gush [16] and theoretically by Boissoles et al. (see Ref. [17], and references cited therein). At the other end of the spectrum, in the deep-ultraviolet, absorption features were observed, that were in part ascribed to O_2-O_2 resonances [18].

Theoretical treatment of oxygen and its dimer dates back to 1924 when Lewis proposed the existence of a weak chemical bond establishing an O_4 molecule that would not be paramagnetic

[19]. While Lewis focused on the spin aspects, Pauling singled out the O_4 molecule for its exceptionally strong Van der Waals forces, that might give rise to a chemical bond [20]. Thus, ab initio calculations on the oxygen dimer are complicated by the fact that both the Van der Waals interaction and the spin interactions between two paramagnetic molecules play a role. The O_2 triplet ground state gives rise to singlet, triplet and quintet states in the dimer, therewith giving rise to a system with fine structure splittings [21]. Further complications arise from tunneling through internal barriers [22]. Calculations of full potential energy surfaces of the O_2-O_2 Van der Waals complex yield minimum energy structures for the singlet and triplet states in a parallel planar D_{2h} geometry at an equilibrium inter-molecular separation of $6.1-6.2a_0$ at binding energies of 154 and $140\,cm^{-1}$ [23]. Later, also ab initio potentials involving electronically excited O_2 were calculated [24]. Such calculations provide a basis for an assignment of the rotational structure in the bound dimer systems [25].

Whether the two O_2 molecules form a bound Van der Waals complex, or are essentially unbound and absorb the photon during a collisional fly-by, has been a matter of discussion in the literature. Low-temperature measurements show some ripple structure—indicating that bound $(O_2)_2$ states play a role in the absorption resonance [7]. Measurements by Biennier et al. [25] and Campargue [26] in a slit-jet expansion have indeed shown many narrow resonances in the oxygen dimer. The latter studies prove that at low temperatures bound states exist, since the resonances are unequivocally associated with bound rotational states of the oxygen dimer. However, these measurements were carried out at the characteristically low final temperatures in molecular expansions, strongly deviating from atmospheric conditions, where the bound states are presumed to play no role. Vigasin and coworker [27–29] have analyzed the contribution of bound and free–free dimers to the absorption in collision-induced spectra, thereby dividing phase space into three compartments, including that of metastably bound dimers in which molecules are slightly bound by a centrifugal barrier. From their thermodynamic model it follows that even at temperatures as low as 150 K bound complexes do not contribute significantly to the collisional spectral features [30].

Obviously, the oxygen CIA resonances are of importance for atmospheric physics. The oxygen collisional complex is held responsible for a non-negligible fraction (1–2%) of the absorption of solar radiation [31,32]. The cross sections of the O_4 features depend quadratically on pressure, and they are particularly useful to determine cloud top heights in the lower atmospheric layers. Acarreta et al. [33] have introduced a cloud detection algorithm, which also yields the effective cloud fraction within a ground pixel, using the O_2-O_2 resonance at 477 nm. This resonance falls within the spectral window (270–500 nm) sampled by the Ozone Monitoring Instrument (OMI) aboard the EOS-Aura satellite, which was launched in summer 2004 with the aim to detect global ozone columns. Using Ref. [34] it is estimated that a 10% error in the peak absorption of the 477 nm O_2-O_2 resonance leads to errors of about 1 km in the retrieved cloud altitude. This, in turn, leads to an error of about 1% in the total column density of ozone. As the target accuracy of the total ozone column is about 1%, which is needed to detect trends in ozone and to detect tropospheric pollution, errors in the peak absorption of O_2-O_2 should not be larger than 5%. Since the scatter in the literature values on the band integrated CIA cross section amounts to 15%, the uncertainty in the retrieved ozone column densities from OMI for cloudy measurements is dominated by the uncertainty in the O_2-O_2 resonance; the cloud-free uncertainty is 1.2% and is mostly due to instrument noise.

The above-mentioned relation to ozone retrieval warrants detailed and accurate laboratory measurements to provide the integrated cross section and shape function of the O_2-O_2 resonances. In the distant past Tabisz et al. [35], McKellar et al. [36] and Ewing and coworkers [6,7] determined absorption cross sections for both the 477 and 577 nm resonances at a number of temperatures. Recently, studies were performed by Newnham and Ballard [37] and Hermans et al. [38] applying Fourier-transform spectroscopy, and Morville et al. [39] as well as Tiedje et al. [40], who performed cavity ring-down measurements. As a continuation of previous studies in our laboratory on O_2-O_2 cross sections at room temperature [2,41] we have built a special cell to carry out cavity ring-down experiments at controlled low temperatures in the range 184–294 K. In view of the relevance for ozone column density retrieval, as discussed above, the focus has been on the 477 nm O_2-O_2 feature, but also new data were collected for the 577 nm resonance.

2. Description of the setup and the experimental procedure

2.1. CRD-setup and the pressure-ramp method

The present laser-based cavity ring-down measurements at low temperatures are an extension of previous investigations on O_2-O_2 at room temperature [2,41]. The ring-down cell, especially constructed for the purpose of controlled low-temperature measurements (see Fig. 1), is built from two highly reflective mirrors (Research Electro Optics) with a diameter of 25.4 mm, radius of curvature of 100 cm and a reflectivity of $\mathscr{R} \approx 99.99\%$ (one set coated for 470 nm and one for 580 nm), leading to typical decay times of $\sim$30 µs in the cavity with length $d = 80$ cm. A special methodological feature in our studies is the application of the pressure-ramp method, that was
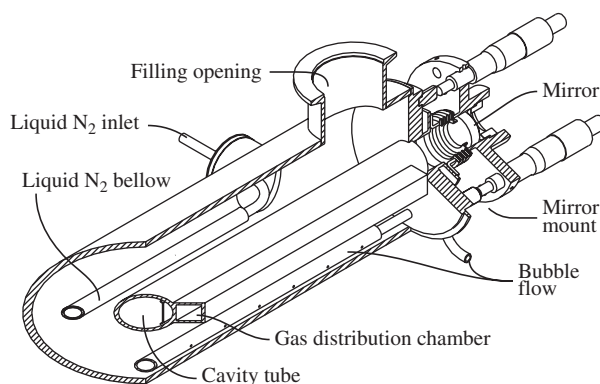

Fig. 1. Three-dimensional drawing of the cell used for the present low-temperature CRD measurements. The coolant liquid (ethanol, acetone or anti-freeze) is poured into the outer volume and then cooled by liquid nitrogen flowing through the bellow. Oxygen, freed from aerosols and pre-cooled by letting it pass through two sintered steel filters, first enters a gas distribution chamber alongside the ring-down inner cavity. To ensure a homogeneous distribution and a monotonic increase of gas density at the laser beam path, the oxygen enters the inner cell via a number of holes connecting the gas distribution chamber and the inner cell. The micrometer screws and bellows between the mirrors and the rest of the cell allow for careful alignment. Dry nitrogen is blown against the outside of the mirrors to keep them free from ice.

first applied to quantitatively assess the cross sections for Rayleigh scattering by Naus and Ubachs [42]. This method implies that the cell is first evacuated and then slowly filled with oxygen, while the loss rate in the cavity and the pressure in the cell are continuously monitored. In Fig. 2 typical examples of such pressure-ramp curves are displayed at various frequency positions on the 477 nm resonance, displaying different quadratic contributions to the loss rate.

The frequency and pressure-dependent loss in the cavity contains three terms: an offset representing the frequency-dependent reflectivity of the mirrors (or background), a linear contribution associated with Rayleigh scattering and a quadratic contribution representing the bi-molecular or CIA:

$$\beta_{\bar{\nu}}(N)/c = \beta_{\bar{\nu}}^0/c + \sigma_{\bar{\nu}}^{\mathrm{R}} N + \alpha_{\bar{\nu}}^{\mathrm{CIA}} N^2, \tag{1}$$

with c the speed of light, $\sigma_{\bar{\nu}}^{\mathrm{R}}$ the Rayleigh scattering cross section, N the number density and $\alpha_{\bar{\nu}}^{\mathrm{CIA}}$ the CIA cross section. The decisive advantage of this pressure-ramp method, whereby pressure-dependent measurements are performed at each fixed-frequency position, is that the background, the Rayleigh scattering and the true collisional contribution can be disentangled. In addition to the terms in Eq. (1) higher-order terms may play a role in principle, e.g. as a result of tertiary collisions. Based on the findings of Tabisz et al. [35] and others (see below) such features are insignificant at subatmospheric pressures, as used in the present investigation.

A Nd:YAG pumped pulsed dye laser system (Quanta-Ray PDL-3) is used for the ring-down measurements. For the blue region (477 nm resonance) 355 nm pumping of Coumarine-480 dye is routinely employed, while for the yellow range Rhodamine-B is pumped by the 532 nm output of the Nd:YAG laser. As discussed in literature (see, e.g. Ref. [43]) the determination of cross
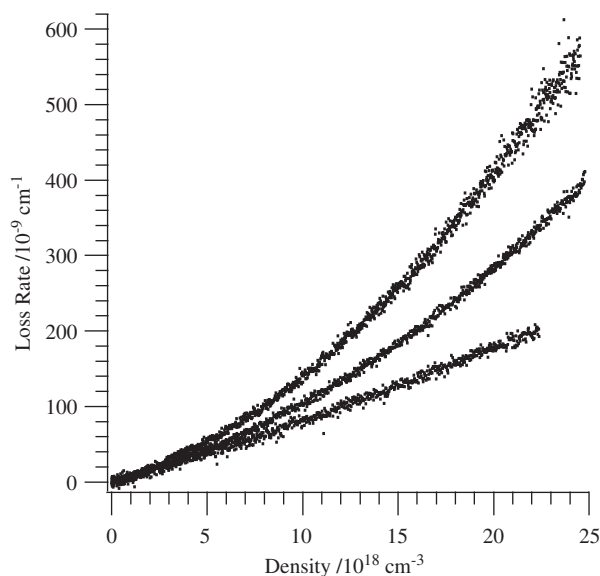

Fig. 2. Three typical pressure ramps, recorded for different frequencies at room temperature on the 477 nm resonance. From top to bottom the positions of the traces were 20 951 cm^{-1} (near the top of the resonance), 20 137 cm^{-1} (in the red-wing) and 21 392 cm^{-1} (in the blue-wing, practically off-resonance). The offset due to the mirror-reflectivity has been removed for clarity.

sections in CRD experiments is hampered by the linewidth problem, giving rise to multi-exponential decays on narrow resonances. But here the opposite is the case: the resonances are almost as wide as the gain profiles of the dyes. The principle of CRD detection makes the measurements independent of laser pulse intensity, hence the linewidth problem poses no specific problems in the present experiments. Only when the laser wavelength is tuned to the wings of the dye gain curve appreciable amounts of amplified spontaneous emission (ASE) can be produced in the dye laser, which may result in systematic offsets in the measured cross sections. In our experiments this was the case on the short-wavelength edge of the 477 nm resonance. At these wavelengths additional measurements were performed with Coumarine-460 dye, thus producing a reliable set of ring-down transients at these wavelengths.

2.2. Reaching and maintaining low temperatures

The lowest temperatures are obtained by submerging the CRD cell (see Fig. 1) in a low-temperature bath, consisting of a solid–liquid mixture of acetone—which has a freezing point of $-94.8\,^{\circ}$C or 178.4 K. Since liquids undergo a first-order phase transition at the freezing point, the cell can be reasonably well stabilized at that temperature. Usually, an equilibrium temperature is established slightly above the freezing point; for that reason the 477 nm resonance was investigated at 184 K and the 577 nm resonance at 190 K, when using acetone as a coolant. The measurements at 268 K (only for the 577 nm O_2-O_2 feature) were performed with a different cooling technique; here, a chiller filled with anti-freeze (1,2 ethane-diol/ethylene-glycol mixture) was used to bring down the temperature. The filler opening and the bubble-flow pipes were used as the connection points for the hoses, and the chilled liquid was pumped around by the chiller. The lowest temperature reached with the chiller was 268 K ($-5\,^{\circ}$C). A separate series of measurements was performed (only for the 477 nm O_2-O_2 feature) at a temperature of about 230 K ($-45\,^{\circ}$C) using the anti-freeze mixture as coolant. Similar to the experiments using acetone, the anti-freeze mixture was frozen by flushing liquid nitrogen through the bellow. Due to the lack of a latent heat step at the freezing-point phase transition, difficulties were encountered in keeping the temperature at a constant value, but eventually controlled measurements at a temperature of 230 ± 5 K could be performed. For the 477 nm resonance again a large set of data was taken at room temperature, therewith verifying previous results by our team [41] taken in a different cell. The results were analyzed and are included in this paper. For the 577 nm resonance no additional room temperature measurements are added.

After the cell is aligned and evacuated, the outer volume is filled with the coolant to a level well above the ring-down cell. Liquid nitrogen is then flowed through a bellow, cooling down the coolant substance, in which the actual ring-down cavity is immersed. For the coolants used, frozen parts will sink to the bottom of the outer volume. To ensure a homogeneous temperature throughout the cell, and to bring the coldest coolant into contact with the ring-down cavity, nitrogen gas is blown through a tube with a series of holes located at the bottom of the outer volume. To reduce the heat load of this gas-flow, the nitrogen gas is cooled down by leading it through another container with liquid nitrogen. The bubbles will mix the liquid and bring the temperature of the entire cell down to the freezing point of the coolant. Reaching the freezing point of acetone takes between 4 and 5 h, and after this time the temperature can be maintained by keeping a steady flow of liquid nitrogen through the bellow. A specific advantage of the present

cell is that the low temperature is maintained homogeneously over almost the entire length of the cavity; even the mirror mounts are in contact with the coolant.

2.3. Measurements

As with the measurements at room temperature [2,41], the CIA cross section is determined with the pressure-ramp method. To fill the cell with oxygen at a predetermined low temperature, the gas is purged through a sintered stainless steel filter with 7 μm pores, located inside the outer tube and submerged in the coolant. This filter provides a large contact surface area, and after purging, the temperature of the gas is assumed to be the same as that of the fluid. Because this thermalization filter is inaccessible from the outside, a second filter with 0.5 μm pores is used outside the cell to filter aerosols from the oxygen and prevent contamination of the thermalization filter. Apart from this filter, oxygen with a specified purity of 99.999% is used without further treatment. The rate of flow is controlled by a needle valve and set for the pressure ramps to last about 15 min. The temperature of the coolant is measured by a thermocouple—type K (Ni + 10% Cr) against (Ni + 2% Al + 2% Mn + 1% Si)—with the tip placed close to the oxygen thermalization filter. A pressure sensor is placed in the top part inside the cell, in an effort to reduce the heat load on the system. The capacitance baratron for the range 0–1333 hPa has an uncertainty of 2 hPa. The oxygen gas density is calculated from the measured temperature and pressure using the Van der Waals equation of state. During the pressure ramps the ring-down times (or loss rates $\beta_{\bar{v}}$) are constantly monitored at a 10 Hz repetition rate, by methods described by Naus et al. [43], while also the pressure and temperature measurements are continuously stored in the data-handling computer.

The measurements are performed after the ring-down cell is aligned to yield single exponential decays. As discussed in Ref. [43] only under such conditions can the characteristic retrieved ring-down times be interpreted in terms of cross sections. In the first step of the measurement and data analysis an exponential decay function is fitted to the ring-down transients. This results in typical density-ramp traces as shown in Fig. 2 for some measurements on the 477 nm resonance.

As in the previous measurements [2,41], the wavelength of the laser was measured after each CRD-pressure ramp at a fixed wavelength position, with an echelle-grating spectrometer yielding an absolute accuracy of 0.2 cm^{-1}.

2.4. Data analysis

The density-ramps are fitted with a second-order polynomial, as given by Eq. (1). In a first run the data were subjected to a three parameter fit, from which a fitted value of the linear term is derived. Results for this linear term are displayed in Fig. 3 for several data sets. As the linear terms should coincide with the values for the Rayleigh scattering cross section $\sigma_{\bar{v}}^{R}$, calculated from the refractive index and King correction factor [44], they are a consistency check of the experimental approach. As shown in Fig. 3 the variation of the linear terms from the three parameter fits exhibits a statistically random distribution around the curve representing the calculated value, where the actual variations, in fact, give some insight in the accuracy of the fits. The statistical deviations on the data recorded at the other temperatures were taken as a selection criterion; those
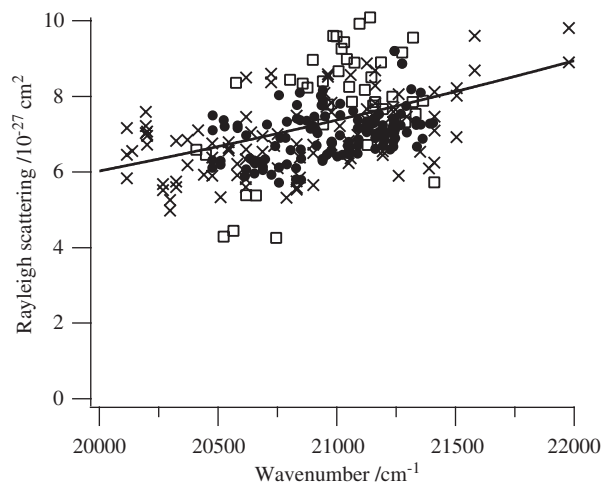
Fig. 3. Fitted values for the linear scattering terms as obtained from three parameters fits for the data sets pertaining to the 477 nm resonance at room temperature (●), at 230 K (×), and at 184 K (□). The full line corresponds to the value of the calculated Rayleigh scattering cross section, $\sigma_{\bar{\nu}}^{R}$, for the specific wavelength.

pressure ramps, where the fitted linear term was off by more than 20% from the calculated $\sigma_{\bar{\nu}}^{R}$ (for room temperature data) or 40% (for the other data) were discarded.

In a second round of fitting (two parameter fits) the linear term is kept fixed at the calculated $\sigma_{\bar{\nu}}^{R}$, which is calculated from the refractive index and King correction factor [44]. Values to be taken for $\sigma_{\bar{\nu}}^{R}$ were discussed in a previous paper focusing on direct Rayleigh scattering measurements [45]. This second round of fitting yields an improved accuracy for the determination of the quadratic term, corresponding to the CIA cross section $\alpha_{\bar{\nu}}^{CIA}$. In Figs. 4 and 5, the final results of the measurements on the 477 and the 577 nm resonances of $O_2 - O_2$ CIAs are shown. The measurements at 294 K on the 577 nm resonance are taken from Naus and Ubachs [2]. The room temperature measurements on the 477 nm resonance stem from new series of measurements in combination with similar data, obtained in a previous investigation [41].

2.5. Further reduction of the data

In Figs. 4 and 5 resulting data for the quadratic components $\alpha_{\bar{\nu}}^{CIA}$ are plotted as a function of frequency. In the same figures fits to the measured data are shown using a model function. The solid lines are the least-square best-fit results. The dashed lines in these figures indicate the confidence interval for the fit-result at the 2σ (95.4%) level. This means that if the experiments were repeated, 95.4% of the sets would yield a fit that falls within the indicated interval. The dotted lines indicate the confidence interval for the prediction at the same level, indicating that 95.4% of the measured points should fall within the indicated band.

Currently there exists no good theoretical description of the $O_2 - O_2$ CIA profile, and empirical model functions are used to describe the shape function of the resonance feature. In principle, the resonance profile could be calculated based on multi-dimensional ab initio potential energy surfaces and dipole moments, with integration over kinetic energy and angular distributions of the vectorial properties (velocities and angular momenta) of the collision partners, but such elaborate
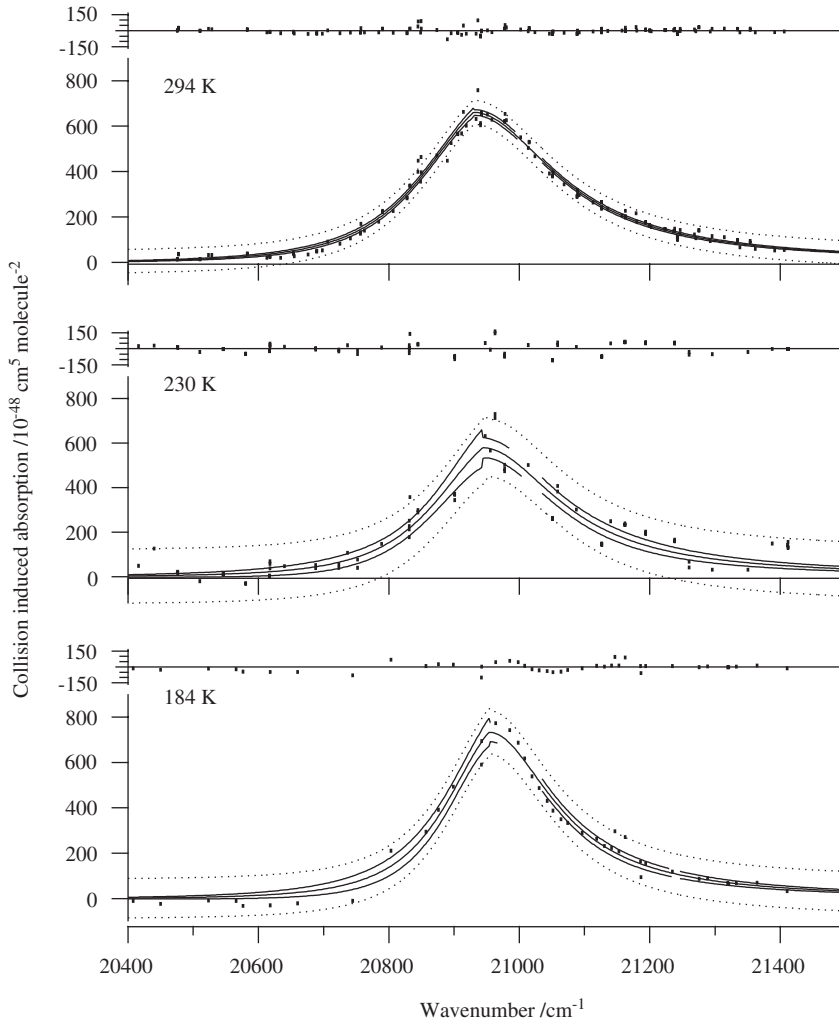
Fig. 4. The absorption profiles of the O_2-O_2 feature near 477 nm at 294 K, 230 K and 184 K. Residuals from a comparison to a model function are shown as well. Further details are given in Section 2.5.

procedures have not yet been attempted. The purpose of representing the shape of the resonance in terms of an analytical representation is twofold: the shape function is used to derive an integrated CIA cross section — $\int_{Band} \alpha_{\bar{v}}^{CIA} \, d\bar{v}$ — and the shape function can be used in retrieval procedures for the determination of column densities and profiles of species in the Earth's atmosphere. The shape function we use to describe the 477 nm resonance was first suggested by Watanabe and Welsh [46], and has been used by several authors [6,35,36]. In this empirical model, the high- and low-frequency wings of the transition show a Boltzmann related ratio:

$$\frac{\mathscr{A}(\bar{v}_c - \Delta\bar{v})}{\mathscr{A}(\bar{v}_c + \Delta\bar{v})} = \exp\left(-\frac{hc\Delta\bar{v}}{k_B T_{eff}}\right), \tag{2}$$
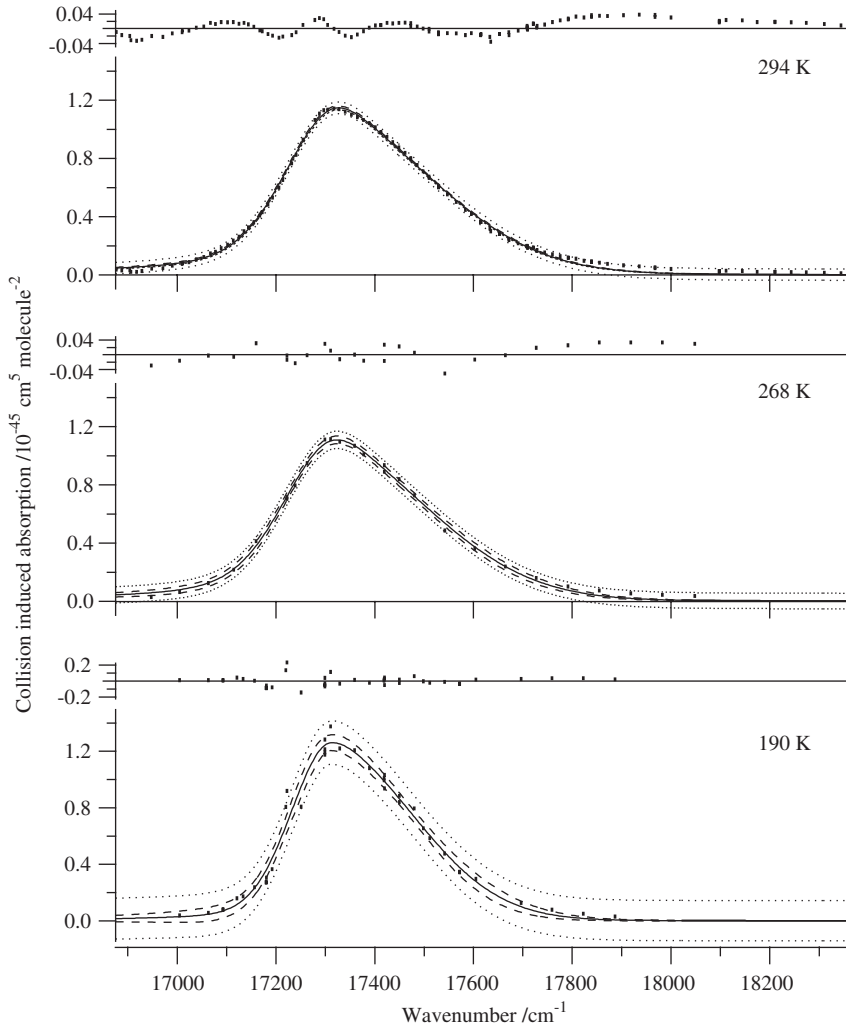
Fig. 5. The absorption profiles of the O_2-O_2 feature near 577 nm at 294 K taken from Ref. [2], 268 and 190 K. Residuals from a fit to a model function as discussed in Section 2.5 are shown as well.

with $\mathscr{A}$ the intensity of the absorption, $\bar{v}_c$ the central position of the absorption resonance, $\Delta\bar{v} = \bar{v} - \bar{v}_c$, T_{eff} the effective temperature of the gas and h, c and k_B are Planck's constant, the speed of light and Boltzmann's constant, respectively.

Eq. (2) does not specify the shape of the profile; it only determines the high- and low-frequency ratios. For the overall shape of the underlying line a Lorentz profile is assumed, leading to

$$\mathscr{A}(\bar{v}) = \frac{a(\Gamma/2)^2}{(\Delta\bar{v})^2 + (\Gamma/2)^2} \times \begin{cases} 1 & \text{if } \Delta\bar{v} > 0, \\ \exp\left(\frac{hc\Delta\bar{v}}{k_B T_{eff}}\right) & \text{if } \Delta\bar{v} \leqslant 0, \end{cases} \tag{3}$$

where a and Γ represent parameters for the amplitude and the width of the absorption feature. In Ref. [41], the temperature in Eq. (3) was taken to be the temperature at which the measurements were performed. Especially at lower temperatures, this leads to unsatisfactory fit results. The effective temperature T_{eff} is now a fit-parameter and it is adjusted to give the best fit to the data.

During the analysis of the data, it became apparent that the model given by Eq. (3) works well for the description of the 477 nm resonance, but when it is applied to the 577 nm resonance, large residuals and a very poor fit are found. Following the analysis of Naus and Ubachs [2], a skewed Voigt profile was used to describe the shape of the 577 nm resonance. The skewed Voigt profile is approximated by a linear combination of a Gauss and a Lorentz profile, where the left- and right-hand sides have a different linear scale:

$$\mathscr{V}(\bar{v}) = (1-b)\frac{a}{1 + [4(\Delta\bar{v})^2/\Gamma^2\xi^2]} + ba\,\exp\left[-4\ln 2\left(\frac{\Delta\bar{v}}{\Gamma\xi}\right)^2\right] \qquad (4)$$

with

$$\xi = \begin{cases} 1 + 2\arctan(\text{skew factor})/\pi & \text{if } \Delta\bar{v} > 0, \\ 1 - 2\arctan(\text{skew factor})/\pi & \text{if } \Delta\bar{v} \leqslant 0 \end{cases}$$

and a and b amplitudes. The parameters found in the fitting procedure are shown in Tables 1 and 2. The two sets use different model functions and therefore have different parameters in their respective tables. The resulting effective temperatures found in the fitting routines using Eq. (3) are systematically and significantly higher than the real measured temperatures of the oxygen gas. Once again we note that T_{eff} should by no means be regarded as a temperature, rather than as a fitting parameter in a model.

The uncertainties indicated are found from the fitting procedure. An attempt was made to propagate the error estimates found from the fit of the ring-down transients, but the resulting errors were unrealistically small. The currently indicated errors assume that the errors in all measured points are equal and that the model function is accurate. In that case χ^2 scaling is

Table 1
Parameters describing the absorption profile of the O_2-O_2 feature near 477 nm at three different temperatures

Temperature (K)	294	230	184
Coolant	None	Anti-freeze	Acetone
$\bar{v}_c$ (cm^{-1})	20929.9 ± 2.8	20943 ± 11	20953 ± 6
λ_c (nm)	477.79 ± 0.06	477.47 ± 0.26	477.25 ± 0.14
FWHM (cm^{-1})	247.1 ± 6.8	228 ± 26	197 ± 14
FWHM (nm)	5.64 ± 0.16	5.2 ± 0.6	4.5 ± 0.3
Γ (cm^{-1})	306.4 ± 6.8	283 ± 26	239 ± 14
a (10^{-48} cm^5 molecule^{-2})	660 ± 6	578 ± 23	733 ± 20
T_{eff} (K)	361 ± 37	331 ± 138	316 ± 102
$\int \mathscr{A}(\bar{v})\,d\bar{v}$ (10^{-42} cm^4 molecule^{-2})	0.234 ± 0.006	0.190 ± 0.022	0.207 ± 0.016

The parameters were found using Eq. (3) as the model function and a least-square fit. The indicated errors are 1σ values. A graphical representation of the data and the fit-result are shown in Fig. 4.

Table 2
Parameters describing the absorption profile of the O_2-O_2 feature near 577 nm at three different temperatures

Temperature (K)	294[a]	268	190
Coolant	None	Chiller	Acetone
$\bar{\nu}_c$ (cm^{-1})	17325.8 ± 1.7	17322.8 ± 3.5	17313 ± 7
λ_c (nm)	577.17 ± 0.06	577.3 ± 0.1	577.6 ± 0.2
FWHM (cm^{-1})	346.5 ± 3.0	342.3 ± 7.1	290 ± 10
FWHM (nm)	11.5 ± 0.1	11.3 ± 0.2	9.6 ± 0.3
Γ (cm^{-1})	318 ± 3	317 ± 7	257 ± 10
a (10^{-45} cm^5 molecule^{-2})	1.15 ± 0.01	1.11 ± 0.03	1.26 ± 0.05
Skew factor	-0.64 ± 0.02	-0.60 ± 0.05	-0.65 ± 0.11
b	0.782 ± 0.012	0.784 ± 0.034	0.91 ± 0.06
$\int \mathcal{V}(\bar{\nu})\,\mathrm{d}\bar{\nu}$ (10^{-42} cm^4 molecule^{-2})	0.470 ± 0.006	0.447 ± 0.013	0.406 ± 0.024

The parameters were found using Eq. (4) as the model function and a least-squares fit. The indicated errors are 1σ values. A graphical representation of the data and the fit-result are shown in Fig. 5.

[a]Measurements taken from Naus and Ubachs [2].

possible and the uncertainties resulting from this procedure are reported. The indicated accuracy on the band integrated absorption cross section is found by applying a Gaussian variation with the indicated standard deviation to the parameters describing the model function and taking the standard deviation of the resulting distribution of integrated cross sections.

3. Discussion and comparison with other measurements

In order to give a complete picture of the measurements of temperature dependence of the collisional $(O_2)_2$ resonances at 477 and 577 nm all available information in literature was collected in conjunction with the presently obtained data. For this purpose, scaling to the appropriate units is required and in some cases digitization of information contained in plotted figures was employed to extract information on three relevant parameters: the peak cross sections, the widths (FWHM) and the integrated cross sections. Final values are included in Figs. 6 and 7. Note here that notwithstanding the fact that the resonance features are clearly asymmetric, widths (FWHM) were determined. The restriction is imposed to collect data obtained from laboratory experiments (in section 3.1), because these are considered to originate from well-controlled experiments. From these data, displayed in Fig. 6 (for the 477 nm resonance) and in Fig. 7 (for the 577 nm resonance) temperature-dependent trends are deduced, which are discussed in Section 3.2. Subsequently, a comparison with data and trends obtained from atmospheric measurements is made in Section 3.3.

3.1. Data collection of laboratory measurements

For both the 477 and 577 nm resonances, Tabisz et al. [35] list the band integrated cross sections at 297 K, but not the widths nor the peak cross sections; those were extracted by digitization
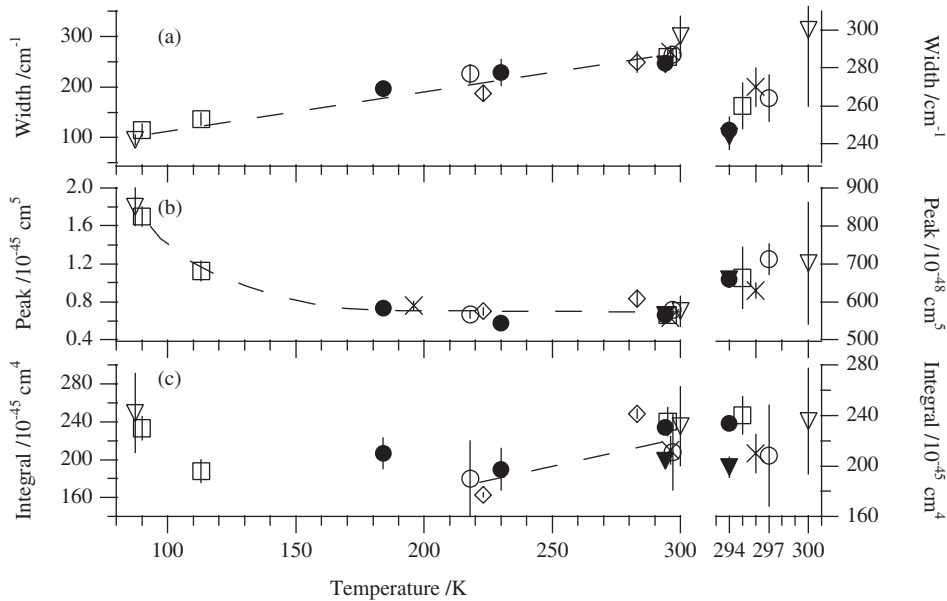
Fig. 6. Temperature dependence for parameters of the 477 nm O_2-O_2 resonance. The width is shown in (a), the height in (b) and the band integrated intensity in (c). The vertical bars indicate the 1σ confidence level on each point. Sources: $\triangledown$—Ewing et al. [6]; $\times$—Greenblatt et al. [5]; $\diamond$—Newnham and Ballard [37]; $\circ$—Tabisz et al. [35]; $\square$—McKellar et al. [36]; $\blacktriangledown$—Hermans et al. [38]; $\bullet$—this work. The sections at the right-hand sides duplicate the data already contained in the main section of the graphs at enlarged scales. The dashed lines are drawn to guide the eye, and to indicate temperature dependences.

procedures. From the work of McKellar et al. [36] all three parameters were deduced from the digitized plots. Blickensderfer and Ewing [6] give the integrated absorption cross sections, the half-widths at 300 and 87 K and the peak heights at 300 and 290 K (at different pressures). The difference between the latter two values is taken as a measure for the error on the peak height. The peak height values at 87 K are taken from a digital readout of the graphs. Greenblatt et al. [5] give some parameters for both resonances; in addition, digitized data of the room temperature measurements in Ref. [5] were obtained via the authors of Ref. [33] from which the band integrated cross section was calculated. Morville et al. [39] give the width and peak height for the 577 nm band at three temperatures. The band integrated values were extracted via the digitized plot, using direct numerical integration. From the noise on the plot, and the baseline seen in the graph, the uncertainty on the integral is estimated to be around 10%. Tiedje et al. [40] give all three values for the 577 nm band in their paper. Newnham and Ballard give the peak absorption cross section and the integrated absorption cross section plus the error estimate for both resonances at two temperatures in Tables 6 and 7 of their paper; a value for the FWHM value was deduced by us from their raw data [37]. Finally, Hermans et al. [38] performed Fourier-Transform measurements at pressures in the range 0.3–1 bar, applying multi-passing in a 50 m cell at room temperature. Values for the peak cross sections and the widths are obtained from Table 3 in Ref. [38], while a value for the integrated cross section is obtained from the raw data. These raw
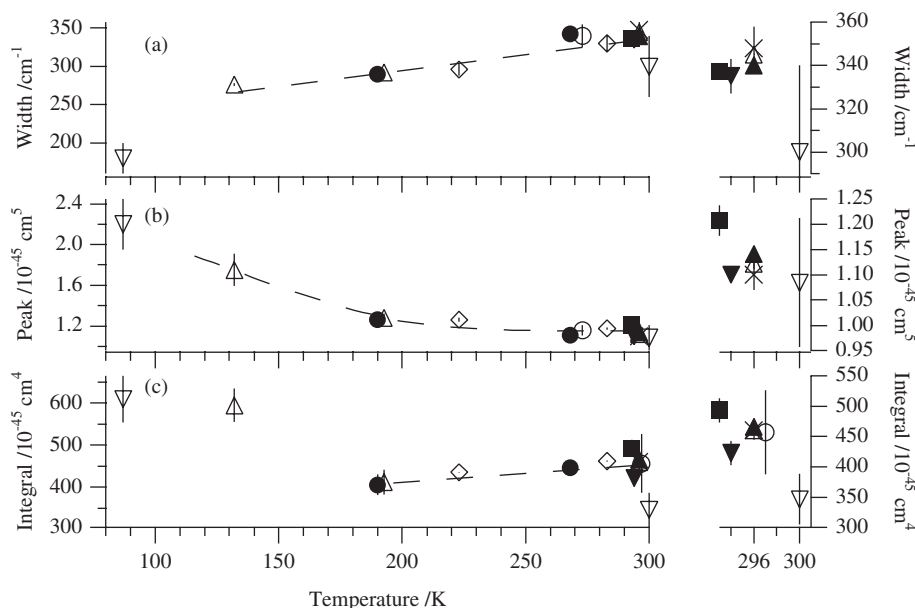
Fig. 7. Temperature dependence for parameters of the 577 nm O_2-O_2 resonance. The width is shown in (a) the height in (b) and the band integrated intensity in (c). The vertical bars indicate the 1σ confidence level on each point. Sources: △—Morville et al. [39]; ◇—Newnham and Ballard [37]; ▲—Naus and Ubachs [2]; ▽—Ewing et al. [6]; ■—Tiedje et al. [40]; □—McKellar et al. [36]; ○—Tabisz et al. [35]; ×—Greenblatt et al. [5] ▼—Hermans et al. [38]; ●—this work. The sections at the right-hand sides duplicate the data already contained in the main section of the graphs at enlarged scales. The dashed lines are drawn to guide the eye, and to indicate temperature dependences.

data, in combination with the margins indicated in Ref. [38], were also used to derive an estimate for the uncertainty.

The data near-room temperature are too congested to obtain a clear picture of the asymptotic values. For this reason, the room temperature region for this feature is enlarged in the right hand side of Fig. 6. Hence, this part duplicates the data between 292 and 300 K already contained in the main section of the graphs, while also the vertical scale is appropriately enlarged. The same is done for the data on the 577 nm resonance in Fig. 7.

The focus in the present study is on the collision-induced cross section, which scales, according to Eq. (1), with the density squared N^2, and it should not depend on the range of pressures or densities at which the measurements are performed. The quadratic dependence on pressure was verified for a number of O_2-O_2 CIA features, including the 477 and 577 nm resonances, in early work by Tabisz et al. [35], and by Dianov–Klokov [4] for pressures up to 35 bar, while Greenblatt et al. followed the quadratic pressure dependence of the 577 nm resonance up to 55 bar [5]. In the data collection from previous measurements a number of sets are used, that are recorded at elevated pressures. In the following, all data sets are compared without further reference to the actual pressures at which the data were recorded. It is noted again that the present results on the CIA cross sections, obtained with the pressure-ramp method, relate to pressures throughout the range 0–1 bar.

3.2. Temperature-dependent trends

A comparison of results on the CIA features should be based on the entire band profiles including the particular shapes of the resonances. Since detailed information on the actual shapes in previous investigations is sparse and difficult to extract, we have chosen to represent the profiles in terms of three parameters: the peak and integrated cross sections and the widths (FWHM), even though the profiles are definitely asymmetric. As discussed, there exists no closed theory for the band shapes of the CIA O_2-O_2 features and the two different functions given by Eqs. (3) and (4) are just phenomenological parametrizations of the shapes observed.

In Fig. 6, all available information on the collision-induced 477 nm resonance is contained and some unequivocal conclusions can be drawn from it. The width (FWHM) of the resonance exhibits a monotonic increase in the entire temperature range 87–300 K from 100 cm^{-1} at the lowest temperature to 245 cm^{-1} at room temperature. All data points fall close to the dashed lines, serving as an indicator for the temperature dependence. For the room temperature value of the width we have taken the average value of the present investigation and that of Hermans et al. [38] (yielding 244 ± 7 cm^{-1}). These data were recorded at lower pressures, while the other data at room-temperature conditions correspond to high-pressure measurements. As discussed by Blickensderfer et al. [6] elevated pressures may give rise to additional broadening.

The peak cross section of the 477 nm feature sharply drops when departing from the lowest temperature, then leveling off asymptotically to the room temperature value of $(660 \pm 6) \times 10^{-48}$ cm^5 molecule^{-2}. The latter value is obtained from a weighted fit on the set of data available on (near)-room temperature measurements, comprising the present value and literature values. Again the trend is indicated by a dashed line drawn in section (b) of Fig. 6. Based upon the entire set of available data no definite statement can be made on the temperature trend in the atmospherically relevant domain of 200–300 K. However, for a subclass of investigations, where measurements were performed at varying temperatures under otherwise similar measurement conditions, such a statement can be made. In the present series of measurements, using CRDS, a peak cross section is measured at 230 and at 294 K yielding a clear indication of an *increase* of 14 ± 5 % over this temperature interval. Similarly, Newnham and Ballard find an increase, even more pronounced, from their recent FT-spectroscopic measurements [37]. Notwithstanding the fact that the two most accurate and most recent data sets indicate an increase in the peak cross section at atmospheric temperatures the dashed line in section (b) of Fig. 6 shows a constant temperature behavior in this range, thus reflecting the entire manifold of data sets available.

The combination of these trends in the widths and peak cross sections results in a minimum for the integrated cross section lying somewhat near 225 K. As a further consequence, the integrated cross section exhibits an increase in the 200–300 K range; this trend is again indicated by the dashed line in section (c) of Fig. 6. In view of the spread in the data it is difficult to extract a value for the room temperature integrated cross section with a reliable error estimate; an unweighted fit on the entire data set yields $(2.21 \pm 0.17) \times 10^{-43}$ cm^4 molecule^{-2}.

Without going into the details of the temperature dependences of the essential features of the 577 nm resonance as extensively, the dashed lines inserted in Fig. 7 indicate the same trends: an increase of the width toward higher temperatures and a clear indication of an increase of the integrated cross section, at least in the atmospherically relevant range 200–300 K. Also here the

integrated cross section exhibits a dip near 200 K, even clearer than in the case of the 477 nm resonance. For the peak height again a clear overall decrease is found from the lowest temperatures toward room temperature. In the atmospherically relevant range, between 200 and 300 K, this trend appears to be sustained (i.e. shows a slight decrease) in contradiction to the case of the 477 nm feature. Averaging over all available information yields the following values for the 577 nm resonance at room temperature (294 K): width $340 \pm 6 \, \text{cm}^{-1}$, peak cross section $(1.14 \pm 0.15) \times 10^{-45} \, \text{cm}^5 \, \text{molecule}^{-2}$ and integrated cross section $(4.66 \pm 0.15) \times 10^{-43} \, \text{cm}^4 \, \text{molecule}^{-2}$.

3.3. Trends derived from atmospheric measurements

Absorption peak cross sections for various O_4 bands including the 477 and 577 nm bands have also been derived using atmospheric measurements. Both ground-based [10] and balloon-based [9] measurements have been performed, the latter also providing temperature-dependent peak cross sections. Although these atmospheric measurements are obtained under less-controlled conditions compared to laboratory measurements, the derived peak cross sections are comparable to the ones presented here. However, some notable differences are observed as well. The temperature-dependent data from Pfeilsticker et al. [9] yield two major conclusions: (a) the band shapes do not change with temperature, nor with pressure; (b) the peak intensities exhibit a decrease of 11% in the atmospherically relevant temperature domain of 200–250 K. In comparison, the full set of laboratory measurements presented in Fig. 6(a) shows a marked monotonic increase in the width of the resonance over the entire temperature range. The fact that Pfeilsticker et al. observe no change in absorption band shapes for any of the O_4 absorption bands may result from the coarser spectral resolution in the balloon-borne measurements. The situation for the peak intensity on the 477 nm resonance is less unambiguous. When all laboratory values are included, the average in the 200–300 K range indeed yields a constant value, represented by the dashed line in Fig. 6(b). In view of the large spread a 11% decrease in the 200–250 K range may be accommodated. However, the two most recent data sets (the present one and the one of Ref. [37]) suggest an increase in the peak intensity over that range. It is not excluded that the peak cross section exhibits an even more fine-tuned structure with a decrease in the range 200–250 K (in agreement with the findings of Ref. [9]), a minimum somewhere in the range 250–270 K (in agreement with the behavior of the pair distribution function, see below) and again an increase toward room temperature (in agreement with the present findings and those of Ref. [37]).

3.4. On a model for the observed temperature trend

The observation of a minimum in the temperature dependence of the integrated absorption cross sections of O_2–O_2 collision-induced resonances at a certain intermediate temperature is similar to recent findings by Baranov et al. [14], who investigated the CIA spectrum of the O_2 fundamental (vibrational) band near 6 μm. In that specific case, the minimum occurs near $T = 270$ K, while minima in the temperature dependences of the CIA features associated with electronic excitation are found near 225 K (for 477 nm) and 200 K (for 577 nm). Vigasin [30] has discussed this behavior in a simple semi-quantitative model, arguing that the integrated cross section of CIA features in the region of dipole-forbidden transitions is built from two distinctive contributions. On the one hand, in the lower temperature regime, the main contribution stems

from molecular pairs in the vicinity of the minimum $R = R_e$ of the intermolecular potential. On the other hand, in the regime of high temperatures, in which all vibrational states in the intermolecular potential are populated, absorption occurs at intermolecular separations near the repulsive branch of the potential. Invoking parameters associated with a simple Lennard–Jones potential, a parabolic temperature dependence is derived exhibiting a minimum near 270 K for the CIA fundamental. Qualitatively these arguments may be transferred to the case of electronic excitation of collision partners as well, explaining the parabolic behavior in the integrated cross section. The behavior of the integrated absorption coefficient with its minimum at intermediate temperatures may thus be associated with the temperature dependence of the pair distribution function. A differing location of the minimum can then be ascribed to the fact that the intermolecular potential for the electronically excited final state is different.

More detailed and quantitative calculations, based on true and multi-dimensional potentials, may reveal whether such an explanation is correct. Full ab initio calculations may also provide insight into the cross sections of the various CIA oxygen features. An outstanding issue is the question why the 577 nm resonance is so strong. This CIA resonance excites one of the molecules into a $v = 1$ state, and from the perspective of monomer absorption this excitation is associated with a small Franck–Condon factor. Hence, the symmetry-breaking effect must be large in case of the 577 nm resonance.

4. Conclusion

Cavity ring-down experiments have been performed on the O_2–O_2 CIA features at 477 and 577 nm at various temperatures in the range 184–294 K, employing the pressure-ramp method, whereby the linear Rayleigh scattering contribution to the extinction can be separated from the quadratic CIA contribution. The presently obtained data for the temperature-dependent cross sections are included in a compilation of relevant previously obtained data. From the entire set of laboratory data trends are derived in the parameters (widths, peak and integrated cross sections) for both CIA resonances that bear relevance for the use of the data for future satellite monitoring in the Earth's atmosphere.

Of particular importance is the finding that both resonances appear to exhibit a minimum in the integrated cross section, associated with a slow increase in the atmospherically relevant temperature domain 200–300 K. Furthermore, both resonances exhibit a linear increase in their width, a marked and strong effect that is quantified. As for the peak intensity on the cross section a clear decrease is found in the low-temperature region (100–200 K), but the effect is less pronounced in the atmospherically relevant region. In the case of the 477 nm resonance, neither a significant decrease nor increase of the peak cross section is found, when all laboratory data are included in a trend analysis. However, the present study reveals a clear indication of an increase in the peak cross section from measurements at atmospherically relevant pressures (0–1 bar) and at varying temperatures recorded by the same instrument. Herewith, we validate the independent finding by Newnham and Ballard from FT-spectroscopic measurements [37]. The combined set of results provides a better constraint on the parameters (width, peak and integrated cross section) and temperature trends for the O_2–O_2 features and should help improve Earth observation studies.

The present study marks progress in the laboratory investigation of CIA resonances in oxygen, but the goal of producing a set of parameters describing the cross sections at the 1–5% accuracy level has not yet been achieved. Therefore it remains an important issue to perform extended laboratory measurements, using both independent techniques of CRD-spectroscopy and FT-spectroscopy, at a larger set of temperatures leading to an undisputed set of temperature-dependent CIA parameters. Also, above room temperature measurements may be useful to establish unequivocal temperature dependencies. Validation of the temperature dependencies by ab initio quantum chemical methods to support the experimental findings on profiles and cross sections may be useful as well.

Acknowledgements

References

[1] Ellis J, Kneser H. Kombinationsbeziehungen im Absorptionsspektrum des flüssigen Sauerstoffes. Z Phys 1933;86:583–91.

[2] Naus H, Ubachs W. Visible absorption bands of the $(O_2)_2$ collision complex at pressures below 760 Torr. Appl Opt 1999;38:3423–8.

[3] Janssen J. Analyse spectrale des elements de l'atmosphere terrestre. C R Acad Sci A 1885;101:649–51.

[4] Dianov-Klokov VI. Absorption spectrum of oxygen at pressures from 2 to 35 atm in the region 12 600 to 3600 Å. Opt Spectrosc 1964;16:224–7.

[5] Greenblatt GD, Orlando JJ, Burkholder JB, Ravishankara AR. Absorption measurements of oxygen between 330 and 140 nm. J Geophys Res 1990;94:18577–82.

[6] Blickensderfer RP, Wing GE. Collision-induced absorption spectrum of gaseous oxygen at low temperatures and pressures. II. The simultaneous transitions $^1\Delta_g + {}^1\Delta_g \leftarrow {}^3\Sigma_g^- + {}^3\Sigma_g^-$ and $^1\Delta_g + {}^1\Sigma_g^+ \rightarrow {}^3\Sigma_g^- + {}^3\Sigma_g^-$. J Chem Phys 1969;51:5284–9.

[7] Long C, Ewing G. Spectroscopic investigation of Van der Waals molecules. I. The infrared and visible spectra of O_4. J Chem Phys 1973;58:4824–34.

[8] Perner D, Platt U. Absorption of light in the atmosphere by collision pairs of oxygen $(O_2)_2$. Geophys Res Lett 1980;7:1053–6.

[9] Pfeilsticker K, Bösch H, Camy-Peyret C, Fitzenberger R, Harder H, Osterkamp H. First atmospheric profile measurements of UV/visible O_4 absorption band intensities: implications for the spectroscopy, and the formation enthalpy of the O_2-O_2 dimer. Geophys Res Lett 2001;28:4595–8.

[10] Wagner T, von Friedeburg C, Wenig M, Otten C, Platt U. UV—visible observations of atmospheric O_4 absorptions using direct moonlight and zenith-scattered sunlight for clear-sky and cloudy sky conditions. J Geophys Res 2002;107:4424.

[11] Aquilanti V, Ascenzi D, Bartolomei M, Cappelletti D, Cavalli S, Vitores M, et al. Molecular beam scattering of aligned oxygen molecules. The nature of the bond in the O_2–O_2 dimer. J Am Chem Soc 1999;121:10794–802.

[12] Aquilanti V, Ascenzi D, Bartolomei M, Cappelletti D, Cavalli S, Vitores M, et al. Quantum interference scattering of aligned molecules: Bonding in O_4 and role of spin coupling. Phys Rev Lett 1999;82:69–72.

[13] Orlando JJ, Tyndall GS, Nickerson KE, Calvert JG. The temperature dependence of collision-induced absorption by oxygen near 6 μm. J Geophys Res 1991;86:20755–60.

[14] Baranov YI, Lafferty WJ, Fraser GT. Infrared spectrum of the continuum and dimer absorption in the vicinity of the O_2 vibrational fundamental in O_2/CO_2 mixtures. J Mol Spectrosc 2005;228:432–40.

[15] Rinsland CP, Smith MAH KSR, Seals jr RK, Goldman A, Murcray FJ, Murcray DG, et al. Stratospheric measurements of collison-induced absorption by molecular oxygen. J Geophys Res 1982;87:3119–22.

[16] Bosomworth DR, Gush HP. Collision-induced absorption in far infrared. Can J Phys 1965;43:751–7.

[17] Boissoles J, Boulet C, Tipping RH, Brown A, Ma Q. Theoretical calculation of the translation–rotation collision-induced absorption in N_2-N_2, O_2-O_2, and N_2-O_2 pairs. JQSRT 2003;82:505–16.

[18] Shardanand. Absorption cross sections of O_2 and O_4 between 2000 and 2800 Å. Phys Rev 1969;186:5–9.

[19] Lewis GN. The magnetism of oxygen and the O_4 molecule. J Am Chem Soc 1924;46:2027–32.

[20] Pauling L. The nature of the chemical bond. Ithaca, NY, Cornell University Press; 1960.

[21] Wormer P, van der Avoird A. (Heisenberg) exchange and electrostatic interactions between O_2 molecules: An ab initio study. J Chem Phys 1984;81:1929–39.

[22] van der Avoird A, Brocks G. The $(O_2)_2$ dimer: magnetic coupling and spectrum. J Chem Phys 1987;87:5346–60.

[23] Bussery B, Wormer PES. A Van der Waals intermolecular potential for $(O_2)_2$. J Chem Phys 1993;99:1230–9.

[24] Bussery-Honvault B, Veyret V. Comparative studies of the lowest singlet states of $(O_2)_2$ including ab initio calculations of the four excited states dissociating into $O_2(^1\Delta_g) + O_2(^1\Delta_g)$. J Chem Phys 1998;108:3243–8.

[25] Biennier L, Romanini D, Kachanov A, Campargue A, Bussery-Honvault B, Bacis R. Structure and rovibrational analysis of the $[O_2(a^1\Delta_g(v=0))_{v=0}]_2 \leftarrow [O_2(X^3\Sigma_g^-(v=0))_{v=0}]_2$ transition of the O_2-dimer. J Chem Phys 2000; 112:6309–21.

[26] Campargue A, Biennier L, Kachanov A, Jost R, Bussery-Honvault B, Veyret V, et al. Rotationally resolved absorption spectrum of the O_2 dimer in the visible range. Chem Phys Lett 1998;288:734–42.

[27] Epifanov SYu, Vigasin AA. Contribution of bound, metastable and free states of bimolecular complexes to collision-induced intensity of absorption. Chem Phys Lett 1994;225:537–41.

[28] Vigasin AA. On the nature of collision-induced absorption in gaseous homonuclear diatomics. JQSRT 1996; 56:409–22.

[29] Epifanov SYu, Vigasin AA. Subdivision of phase space for anisotropically interacting water molecules. Mol Phys 1997;90:101–6.

[30] Vigasin AA. On the temperature variations of the integrated absorption intensity in the oxygen fundamental. J Mol Spectrosc 2004;224:185–7.

[31] Pfeilsticker K, Erle F, Platt U. Absorption of solar radiation by atmospheric O_4. J Atmos Sci 1997;54:933–9.

[32] Solomon S, Portmann RW, Sanders RW, Daniel JS. Absorption of solar radiation by water vapor, oxygen and related collision pairs in the Earth's atmosphere. J Geophys Res 1998;103:3847–58.

[33] Acarreta JR, de Haan JF, Stammes P. Cloud pressure retrieval using the O_2-O_2 absorption band at 477 nm. J Geophys Res 2004;109:D05204.

[34] Private communication with J.F. de Haan (KNMI).

[35] Tabisz GC, Allen EJ, Welsh HL. Interpretation of the visible and near-infrared absorption spectra of compressed oxygen as collision-induced electronic transitions. Can J Phys 1969;47:2859–71.

[36] McKellar A, Rich N, Welsh H. Collision-induced vibrational and electronic spectra of gaseous oxygen at low temperatures. Can J Phys 1972;50:1–9.

[37] Newnham DA, Ballard J. Visible absorption cross sections and integrated absorption intensities of molecular oxygen (O_2 and O_4). J Geophys Res 1998;103:28801–15 The measurements were performed under ESA contract 11340/95/NL/CN, and the raw data are available at URL: ⟨http://www.sstd.rl.ac.uk/sg/Data/O4acs/⟩.

[38] Hermans C, Vandaele A, Carleer M, Fally S, Colin R, Jenouvrier A, et al. Absorption cross-sections of atmospheric constituents: NO_2, O_2, and H_2O. Environ Sci Poll Res 1999;6:151–8.

[39] Morville J, Romanini D, Campargue A, Bacis R. OPO-pulsed CRDS of the visible collision-induced absorption bands of oxygen at low temperature. Chem Phys Lett 2002;363:498–504.

[40] Tiedje H, DeMille S, MacArthur L, Brooks RL. Cavity ring-down spectroscopy of transient O_2-O_2 dimers. Can J Phys 2001;79:773–81.

[41] Sneep M, Ubachs W. Cavity ring-down measurements of the O_2-O_2 collision-induced absorption resonance at 477 nm at sub-atmospheric pressures. JQSRT 2003;78:171–8.

[42] Naus H, Ubachs W. Experimental verification of Rayleigh scattering cross sections. Opt Lett 2000;25:347–9.

[43] Naus H, van Stokkum IHM, Hogervorst W, Ubachs W. Quantitative analysis of decay transients applied to a multimode pulsed cavity ringdown experiment. Appl Opt 2001;40:4416–26.

[44] Bates DR. Rayleigh scattering by air. Planet Space Sci 1984;32:785–90.

[45] Sneep M, Ubachs W. Direct measurement of the Rayleigh scattering cross section in various gases. JQSRT 2004;92:293–310.

[46] Watanabe A, Welsh HL. Pressure-induced infrared absorption of gaseous hydrogen and deuterium at low temperatures. II. Analysis of the band profiles for hydrogen. Can J Phys 1967;45:2859–71.